Acta Materialia 215 (2021) 117093

Contents lists available at ScienceDirect

Acta Materialia

journal homepage: www.elsevier.com/locate/actamat

# Enhancement of vacancy diffusion by C and N interstitials in the equiatomic FeMnNiCoCr high entropy alloy

Eryang Lu[a,1,*], Junlei Zhao[b,1], Ilja Makkonen[a], Kenichiro Mizohata[a], Zhiming Li[c,d], Mengyuan Hua[b], Flyura Djurabekova[a], Filip Tuomisto[a]

[a] Department of Physics and Helsinki Institute of Physics, University of Helsinki, P.O. Box 43, FI-00014, Helsinki, Finland
[b] Department of Electrical and Electronic Engineering, Southern University of Science and Technology, 518055 Shenzhen, China
[c] School of Materials Science and Engineering, Central South University, 410083 Changsha, China
[d] Max-Planck-Institut für Eisenforschung, Max-Planck-Straße 1, 40237 Düsseldorf, Germany

ARTICLE INFO

*Article history:*
Received 8 March 2021
Revised 31 May 2021
Accepted 13 June 2021
Available online 19 June 2021

*Keywords:*
High entropy alloys
Interstitials
Vacancy
Positron annihilation
Density functional theory calculations

ABSTRACT

We present evidence of homogenization of atomic diffusion properties caused by C and N interstitials in an equiatomic single-phase high entropy alloy (FeMnNiCoCr). This phenomenon is manifested by an unexpected interstitial-induced reduction and narrowing of the directly experimentally determined migration barrier distribution of mono-vacancy defects introduced by particle irradiation. Our observation by positron annihilation spectroscopy is explained by state-of-the-art theoretical calculations that predict preferential localization of C/N interstitials in regions rich in Mn and Cr, leading to a narrowing and reduction of the mono-vacancy size distribution in the random alloy. This phenomenon is likely to have a significant impact on the mechanical behavior under irradiation, as the local variations in elemental motion have a profound effect on the solute strengthening in high entropy alloys.



## 1. Introduction

The quest for new metallic alloys with improved properties for withstanding extremely harsh environments has picked up pace in the past decade. Solid solution strengthening that stems from the interaction of lattice dislocations with solutes, is one of the key phenomena employed to tune the mechanical properties [1,2]. However, the typically present negative correlation between strength and ductility in traditional alloys that usually consist of one or two principal alloying elements with dilute (impurity-like) concentrations of other elements, limits material design strategies [3]. High entropy alloys (HEAs) have drawn great interest as they open new frontiers in novel materials design with potentially exceptional mechanical, physical and chemical properties [4–10]. In HEAs, five or more principal elements in (near) equiatomic ratios are usually randomly distributed in a regular crystal lattice e.g., face centered cubic (f.c.c.) or body centered cubic (b.c.c.). The random arrangement of multiple types of atoms at high concentrations results in unique site-to-site lattice distortions (size misfit), and it also leads to a random chemical mixture that brings about locally varying strain distributions (variations in local lattice strain) and atomic-level configurational fluctuations. These features enhance the solute strengthening both geometrically and chemically in the highly concentrated alloys. On the other hand, the cubic structure in single-phase HEAs provides a variety of slip systems that promote ductility, effectively overcoming the strength-ductility trade-off [9,11].

To shed light on the solute strengthening, various theoretical approaches have been employed to analyze the details of strengthening mechanisms in HEAs. An effective-medium-based theory has been proposed by Varvenne et al., [12] in which each elemental component is modeled as a solute embedded in the average effective medium matrix. This model predicts that the local chemical environment and the structural disorder in the random f.c.c. alloy significantly affect the yield strength. Oh et al. [13] introduced the concept of quantum-mechanically derived atomic-level pressure to couple the compositional fluctuations with solute strengthening in single-phase concentrated complex alloys. They suggest that the differences in the charge transfer between neighboring elements drive the configurational fluctuations that dominate the solute strengthening phenomena. These theoretical advances highlight the importance of having a detailed picture of the chemical

* Corresponding author at: Department of Physics and Helsinki Institute of Physics, University of Helsinki, FI-00014, Helsinki, Finland.
*E-mail address:* eryang.lu@helsinki.fi (E. Lu).
[1] These authors contributed equally to this work.

https://doi.org/10.1016/j.actamat.2021.117093

and structural disorder on multiple scales in HEAs for systematically improving design strategies of high-performing materials.

Recently, solid solution strengthening by interstitial introduction has been included in HEA design strategies. The introduction of foreign interstitials, such as C, N, B and/or H, has been found to surprisingly improve the strength significantly without sacrificing the ductility [14–20]. In traditional alloys, foreign interstitials, such as C and N usually induce spatial lattice fluctuations (much higher lattice distortions/local strain distributions than substitutional atoms), affecting the interaction between interstitial species and dislocations [21,22]. In addition, the dilute species are responsible for the formation of carbides and nitrides in the regular lattice, improving the solute strengthening and hardness. From the point of view of lattice defect formation and mobility on the atomic level, the dilute elements are easily trapped by defects or defect clusters and lead to interstitial-vacancy pair formation in traditional alloys [23–25]. The interaction/affinity usually results in a strong binding energy of C or N with vacancies by increasing the migration barriers of vacancy defects. In HEAs, foreign interstitials not only lead to solute strengthening but also present the potential to change the phase stability and stacking fault energies. C atoms have been found by first-principle calculations to stabilize the f.c.c. phase and increase the stacking-fault energy in the Cantor alloy [26]. On the other hand, adding N interstitials significantly enhances the yield strength by increasing lattice frictional stress [27,28]. Moreover, improved phase stability and mechanical properties (higher yield strength and ultimate tensile strength at good ductility) have been observed in C and N co-doped $Fe_{48.5}Mn_{30}Co_{10}Cr_{10}C_{0.5}N_{1.0}$ (at. %) HEA [19,29]. We recently observed that C interstitials introduced into equiatomic FeMnNiCoCr strongly affect the primary irradiation damage formation and suppress vacancy clustering [30]. However, a detailed understanding of the interstitial-controlled mechanisms governing the defect dynamics and mechanical properties requires a better overall picture of atomic-scale interstitial-defect-lattice interactions in HEAs.

In the present work, we have systematically characterized the thermal evolution and recovery kinetics of mono-vacancies created by 6 MeV proton irradiation in equiatomic FeMnNiCoCr (HEA) and C/N interstitial-containing FeMnNiCoCr (iHEA) by positron annihilation spectroscopy [31,32]. We observe unexpected narrowing and reduction of the distribution of directly experimentally determined vacancy migration barriers in the interstitial-containing random alloy. Our state-of-the-art theoretical calculations predict preferential localization of C/N interstitials in Mn and/or Cr rich regions. These regions exhibit the largest lattice distortion distribution without the foreign interstitials. Our results hence suggest that the presence of the C/N interstitials homogenizes some of the fluctuations induced by the chemical disorder in the HEA lattice, with important implications on strengthening mechanisms.

## 2. Methods

### 2.1. Materials and ion irradiation

To avoid any unwanted complex phenomena originating from the material microstructure and from the implanted ion species, we perform our experiments on carefully prepared (homogenized) single-phase HEA and iHEA samples, and irradiate them with 6 MeV protons to very low dose (less than 0.001 dpa) where only mono-vacancy defects are expected [33–35]. The interstitial-free HEA with nominal composition $Fe_{20}Mn_{20}Ni_{20}Co_{20}Cr_{20}$ (at. %) and the iHEA with nominal composition $Fe_{19.8}Mn_{19.8}Ni_{19.8}Co_{19.8}Cr_{19.8}C_{0.5}N_{0.5}$ (at. %) were synthesized in a vacuum induction furnace using pure metals, carbon and $FeCrN_2$ (as the source of nitrogen). The original casts were subsequently hot-rolled, and homogenized at 1200°C for 3 h in Ar atmosphere followed by water-quenching (WQ). According to wet-chemical analysis, the exact C and N contents in the prepared iHEA samples reach 0.60 at. % and 0.81 at. %, respectively, while they are below 0.05 at. % in the HEA samples. The microstructures of both HEAs were characterized by multiple probing methods. Electron backscatter diffraction (EBSD) analysis was performed using a Zeiss-Crossbeam XB 1540 FIB scanning electron microscope (SEM), and X ray diffraction (XRD) measurements were conducted by the X-ray equipment ISO-DEBYEFLEX 3003 in conjunction with Co $K_{\alpha 1}$ radiation [18]. A single f.c.c. phase structure with the average grain size of ~ 200 $\mu$m was obtained in both HEA samples [18]. Sheet specimens with the size of 5 × 5 $mm^2$ were obtained through electrical discharge machining. Electro-chemical polishing was performed on the sheet-like samples from both sides to reduce the thickness to 90 ~ 100 $\mu$m. Figs. 1$a_1$ and $b_1$ present the inverse probe figure (IPF) maps from the EBSD analysis, which reveal the random distribution of grain orientations in the single f.c.c. structure both in HEA and iHEA samples. The f.c.c. structures of as-quenched HEA and iHEA were also examined by XRD analysis as shown in Figs. 1$a_2$ and $b_2$.

All foil-like samples were mounted on an aluminum holder. A 6 MeV proton beam was obtained from the 5 MV tandem Van de Graaff accelerator at Helsinki Accelerator Laboratory, and introduced into the samples at room temperature. The beam current density was kept 800 nA/$cm^2$ (~ 5 × $10^{12}$ ions•$cm^{-2}$•$s^{-1}$), preventing overheating of samples during the irradiation, and samples were irradiated to two different fluences: 5 × $10^{15}$ ions/$cm^2$ and 5 × $10^{16}$ ions/$cm^2$. The 6-MeV proton irradiation-induced damage and ion distribution profiles in the equiatomic FeMnNiCoCr were also predicted by the SRIM-code [36]. No hydrogen is implanted into the samples, and uniform damage is created throughout the thin samples (~100 $\mu$m in thickness), as shown in Fig. 1c. The introduction rate of vacancy defect predicted by SRIM is ~1000 $cm^{-1}$ and the two fluences correspond to 1 × $10^{-4}$ and 1 × $10^{-3}$ dpa (displacements per atom) in the samples. The stopping profile of positrons emitted from $^{22}$Na ($E_{max}$ = 0.545 MeV) in equiatomic HEA is also presented in Fig. 1c, showing that most of the emitted positrons (> 95 %) stop in the 100 $\mu$m thick samples, guaranteeing effective detection and identification of defects.

### 2.2. Positron annihilation spectroscopy

A fast-fast digital positron annihilation lifetime spectrometer with a time resolution of 250 ps is utilized to identify and quantify the atomic scale open-volume defects in the crystalline samples [31]. A $^{22}$NaCl emitter with 1 MBq activity, wrapped in 1.5 $\mu$m thick Al foil, is used as a positron source. The source is sandwiched between two identical sample pieces, and “double sandwich” structure with un-irradiated HEA samples (~ 0.5 mm in thickness) as outside layer is used. The whole package is mounted on a copper sample holder and placed in a vacuum chamber during the temperature-controlled positron lifetime measurements. The irradiated samples were measured at 50 – 600 K by increasing the temperature with 25 K intervals. Each measurement lasted 5 h with ~1 × $10^6$ events collected for the spectrum, Thermal recovery of irradiation-induced defects was observed during the measurements. Above 600 K, isochronal annealing from 650 to 800 K, with 1 h duration and 50 K intervals, was performed on the irradiated samples with positron lifetime measurements performed at RT between each annealing temperature. The corrections for positron annihilation in the source material were determined as 210 ps (2.95 %) and 400 ps (~ 2.2 %), and 0.05 ~ 0.1 % of Ps contribution (1500 ps) was also subtracted from the experimental spectra.

The experimental positron lifetime spectrum is analyzed as a sum of exponential decay components (intensities $I_i$, lifetimes $\tau_i$)

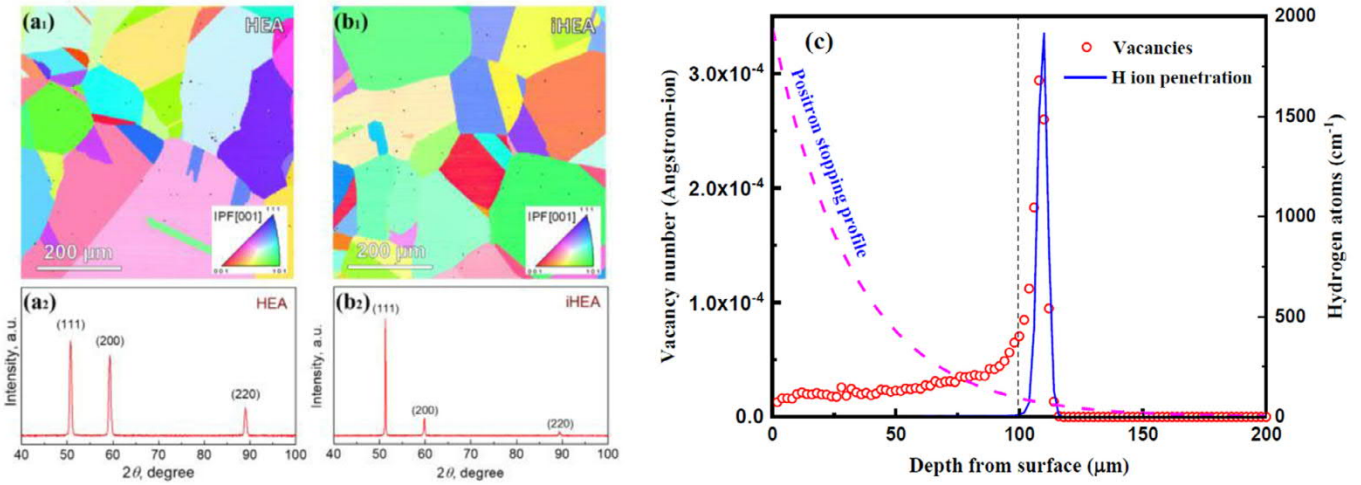


**Fig. 1.** ($a_1$) and ($b_1$) EBSD IPF maps of the quenched HEA and iHEA samples, ($a_2$) and ($b_2$) XRD patterns of the HEA and iHEA samples. (c) SRIM predicted depth profiles of 6 MeV proton irradiation damage, ions distribution and positron stopping profile in the equiatomic FeMnNiCoCr HEA.

[31]. In this work, the spectra obtained in irradiated samples could be analyzed with two components, while un-irradiated samples and post-irradiation annealed samples (above 600 K) only showed a single lifetime component. The shorter lifetime component ($\tau_1$) is the reduced lattice lifetime, and the longer lifetime ($\tau_2$) characterizes a positron trap with open volume. The average positron lifetime ($\tau_{ave}$) is simply defined as: $\tau_{ave} = I_1\tau_1 + I_2\tau_2$, where $I_1 + I_2 = 1$, and it is a statistically accurate parameter as it coincides with the center-of-mass of the lifetime spectrum. In the case of a two-component spectrum representing a case with only one kind of positron trap, the positron lifetimes obtained by fitting the measured spectra are:

$$\tau_1 = \frac{1}{\lambda_B + \Sigma\kappa} \tag{1}$$

$$\tau_2 = \tau_V \tag{2}$$

where $\lambda_B$ is the positron annihilation rate in the lattice and is the inverse of the lattice lifetime $\tau_B$ (often called the bulk lifetime), $\tau_V$ is the positron annihilation lifetime in vacancy defects, and $\kappa$ is the positron trapping rate that is proportional to the defect concentration $C_D$ through $\kappa = \mu C_D$, where $\mu$ is the trapping coefficient.

When two kinds of defects compete in trapping positrons, we employ a positron trapping model with two defects states that best describes the positron behavior in the samples. In this case the average positron lifetime is written as [35]:

$$\tau_{ave} = \frac{\lambda_B\tau_B + \kappa_{st}\tau_{st} + \kappa_V\tau_V}{\lambda_B + \kappa_{st} + \kappa_V} \tag{3}$$

where $\kappa_{st}$ is the trapping rate to structural defects with the annihilation lifetime $\tau_{st}$, and $\kappa_V$ describes the trapping rate to vacancy defects with the annihilation lifetime $\tau_V$. As in the case the single-defect model, the trapping rate to the defect is proportional to its concentration ($C_i$): $\kappa_i = \mu_i C_i$, where $\mu_i$ is the trapping coefficient of the defect. For the vacancy-type defects in f.c.c. metals, we use the trapping coefficient $\mu_V \approx 5 \times 10^{14}\ s^{-1}$, independent of temperature [37]. We model positron trapping to structural defects with a trapping coefficient ($\mu_{st}$) with a temperature dependence of $T^{-n}$ with the experimental value $n$ ranged between 0.5 and 1.5, originating from diffusion-limited trapping [35,38].

In support to the experiments, we calculate the positron lifetimes in defect-free and defected HEAs systems by considering separately the 5 constituent elements as elemental metals in the f.c.c. structure and modeling mono-vacancies in them. This gives us a simple model to understand the possible spread of results that can occur in an alloy environment and approximate the lifetimes in real alloys using weighted averages (see Refs. [2,30] for the idea applied to Doppler broadening in the HEA systems). We use the local-spin-density approximation (LDA) [39] and the projector augmented-wave (PAW) method [40] as implemented in the Vienna Ab-initio Simulation Package (VASP) code [41–43]. The f.c.c. lattice and point defects are modeled using cubic 32-atom supercells. The electron-positron correlation energy and enhancement factor are approximated using the LDA [44]. We use the simplified form of the two-component density-functional theory (DFT) for electron-positron systems, in which a localized positron does not affect the average electronic density, and apply the zero-positron-density limits of the functionals. This scheme has been shown to give results agreeing with more self-consistent modeling. Vacancy defects with trapped positrons are relaxed considering the repulsive force on ions due to the positron [45]. We also modeled the positron lifetime in mono-vacancies in a selection of the randomized 256-atom supercells (see next section).

### 2.3. Modeling of interstitial formation energy and strain distributions

Spin-polarized DFT calculations are conducted using the VASP [41,43,46,47] at the generalized gradient approximation (GGA) level, employing the PAW method [40,42] and the revised Perdew-Burke-Ernzerhof functional for solids (PBEsol) [48,49]. The valence electronic states in the plane wave basis sets are expended with an energy cutoff of 550 eV. For transition metal elements, the 3*p*, 3*d* and 4*s* states are treated as valence states in the PAW potentials while for C and N, the standard 2*s* and 2*p* valent states are considered. Non-spherical contribution of gradient of electronic density is considered. The reciprocal space integration is conducted with a 3 × 3 × 3 Γ-centered Monkhorst-Pack k-mesh grid [50]. The 1st-order Methfessel-Paxton method with the energy smearing width of 0.05 eV is used to describe the partial occupancies of the electronic states. Detailed convergence tests are shown in Supplementary Figure 1. We choose $10^{-4}$ eV and $10^{-3}$ eV as the energy convergence criteria for optimization of the electronic and ionic structures, respectively. The initial magnetic configurations are set as ferromagnetic and are updated collinearly throughout calculations. The final stages are ferrimagnetic configurations, similar to the previous reports [51,52], where Cr and Mn spins are aligned anti-parallel to the Fe, Co and Ni atomic spin. A 256-atom supercell (4 × 4 × 4 conventional f.c.c. cells) is used. Each supercell con-

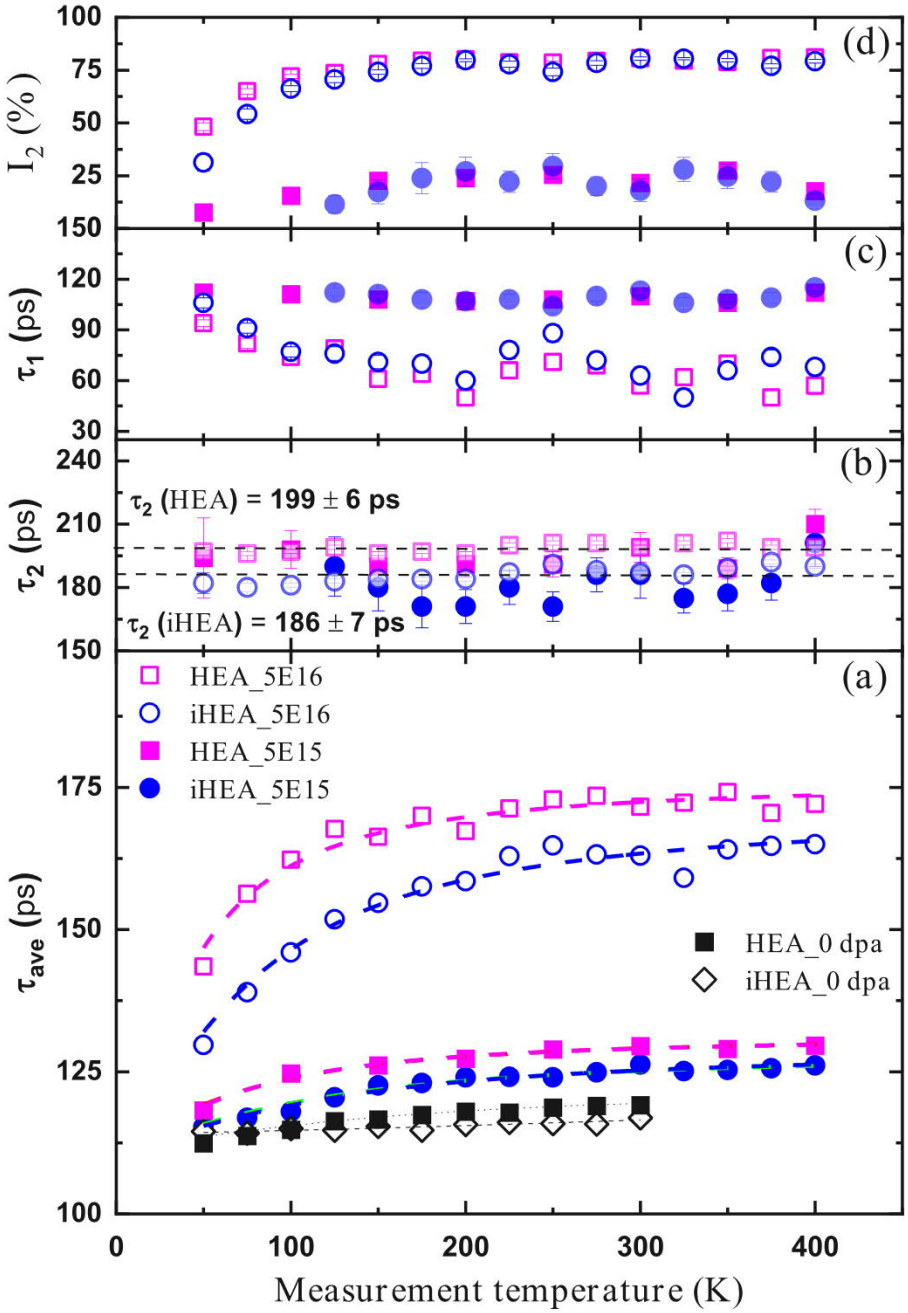


**Fig. 2.** Average positron lifetime ($\tau_{ave}$) in as-grown and irradiated samples as a function of measurement temperature from 50 up to 400 K. The upper panels show the two components $\tau_1$ and $\tau_2$, as well as the intensity ($I_2$) of $\tau_2$ extracted from the temperature-dependent lifetime spectra of irradiated samples. The dashed and dotted curves show the fitting results based on the two-defect state positron trapping model.

sisted 51 Co, 51 Cr, 51 Fe, 52 Mn and 51 Ni atoms, closely resembling the equiatomic composition. In order to consider the effect of local enrichment of certain elements, the chemical disorder is not elaborately unified as the special quasi-random structure (SQS) approach [53]. By directly comparing the local bond disorder of our structure with the SQS cells from the literature [52], we conclude that the lattice distortion is insensitive to the chemical disorder. The atomic configurations are visualized by OVITO [54].

## 3. Results

### 3.1. Irradiation-induced vacancy defects

Fig. 2 shows the positron lifetime obtained in HEA and iHEA samples irradiated to two different fluences with 6-MeV protons ($\phi = 5 \times 10^{15}$ cm$^{-2}$ and $5 \times 10^{16}$ cm$^{-2}$, referred to lower and higher fluence, respectively) as a function of measurement temperature in the range 50 – 400 K. The data for un-irradiated samples are measured in the range 50 – 300 K. At RT, the un-irradiated samples produce a single-component positron lifetime spectrum with average positron lifetime ($\tau_{ave}$) of 119/117 ps (HEA/iHEA notation). In earlier work, the positron lifetime in the lattice (often called the bulk lifetime for historical naming reasons) has been

determined to be in the range $\tau_B$ = 108 – 112 ps based on experiments in the Cantor alloy and FeCoCrNi [2,55,56]. In elemental metals constituting the HEA samples, experimental results have been reported as 110 ps (f.c.c. Ni and b.c.c. Fe) [57,58] and 120 ps (b.c.c. Cr) [59]. We hence assume that the bulk (lattice) lifetime is $\tau_B$ = 110 ps, i.e., slightly shorter than the average lifetime in the un-irradiated HEA and iHEA samples.

In the irradiated samples, $\tau_{ave}$ increases to 130/126 ps at the lower fluence, and to 174/164 ps at the higher fluence. This fluence-dependent increase in $\tau_{ave}$ is a direct indication of open volume defects produced by the irradiation. The increase is less pronounced in iHEA than HEA, indicating that the overall open volume of the defects introduced in the irradiation is smaller in the interstitial-containing samples, in line with our earlier observation of suppressed open volume irradiation damage in iHEA [30]. The separation of the lifetime spectra into two components is shown in Fig. 2 (panels b-d). It is clearly seen that the second (longer) lifetime component is systematically shorter in iHEA ($\tau_2$ = 186 ± 7 ps) than in HEA ($\tau_2$ = 199 ± 6 ps). The shorter component ($\tau_1$) and the intensity $I_2$ of the second component are the same in both HEA and iHEA (for both fluences), except at the lowest temperatures. Hence the difference in $\tau_{ave}$ between irradiated HEA and iHEA originates purely from the value of the second lifetime component and not its intensity. This is a direct indication of the vacancy-type defects created in the irradiation containing slightly smaller open volume on average in iHEA than HEA. At the same time, the concentration of the irradiation-induced defects is the same in both HEA and iHEA with the same irradiation fluence.

Mono-vacancy positron lifetimes in the constituent elemental metals have been experimentally determined for f.c.c.-Ni ($\tau_V$ = 180 ps) [57] and b.c.c.-Fe ($\tau_V$ = 175 ps) [58]. In un-irradiated FeMnNiCoCr samples, lifetime components as originating from mono-vacancies have been reported in the range 170 – 185 ps [55,60], somewhat shorter than in our irradiated HEA and iHEA samples. However, direct comparison is not straightforward as microstructural details and impurity levels are different or unknown. Also, the effect of dislocations on the apparent mono-vacancy lifetime (see below) needs to be taken into account to allow detailed comparison. To estimate the mono-vacancy lifetime that could be expected in HEA, we performed first-principles calculations on elemental metals in the f.c.c. structure (the calculations were validated by calculating also the correct elemental metal structure and comparing to experiments for Ni and Fe). By averaging over the 5 elements and by performing the standard correction of shifting the calculated values by the difference between the calculated and experimentally determined lattice (bulk) lifetimes, we obtain an average mono-vacancy lifetime of $\tau_V$ = 200 ps in FeMnNiCoCr HEA. This coincides with the experimental $\tau_2$ in the irradiated HEA samples, and we hence identify the defects introduced by irradiation as mono-vacancies in the HEA samples. Earlier theoretical calculations [60,61] predict mono-vacancy lifetimes that are slightly shorter than in our modeling, in line with their different approach. Note that mono-vacancies coupled with C interstitials have been found to exhibit a positron lifetime 15 ps shorter than for the pure mono-vacancy in b.c.c.-Fe [58], and we also find shorter $\tau_2$ in irradiated iHEA than in HEA. However, the reduced temperature of thermal recovery (see next section) prevents us from interpreting the positron lifetime in our experiments to originate from mono-vacancy-interstitial complexes in iHEA, as such a complex is by definition more stable than a pure mono-vacancy. We also calculated the mono-vacancy positron lifetimes in a subset of randomized HEA supercells to find that the scatter in lifetimes is 10 ps for various configurations, which corresponds to the range of observed $\tau_2$ in the experiments on the HEA and iHEA samples.

It is clearly seen in Fig. 2 that the average positron lifetime decreases with decreasing temperature (in a reversible manner).

**Table 1**
Positron trapping rates at mono-vacancies, mono-vacancy concentrations and migration barriers extracted from the data in the irradiated HEA and iHEA.

| | $\kappa_V$ ($\lambda_B$) | Vacancy concentration • appm | • cm$^{-3}$ | Vacancy mi- gra- tion bar- ri- ers (eV) |
|---|---|---|---|---|
| HEA_5E15 | 0.32 ± 0.02 | 5.8 | 5 × 10$^{17}$ | 1.6 – 1.9 |
| HEA_5E16 | 2.9 ± 0.1 | 52 | 5 × 10$^{18}$ | 1.6 – 1.9 |
| iHEA_5E15 | 0.34 ± 0.02 | 6.2 | 5 × 10$^{17}$ | 1.63 ± 0.02 |
| iHEA_5E16 | 3.1 ± 0.1 | 56 | 5 × 10$^{18}$ | 1.64 ± 0.02 |

Thermal expansion of the crystal lattice produces at most 0.2 – 1 ps/100 K in $\tau_{ave}$ [35,62], hence the observation is defect-related. Here, the observed temperature dependence strongly suggests diffusion-limited trapping (and hence scattering off, e.g., phonons) that is typical of structural defects such as grain boundaries and dislocations. The temperature-dependent lifetime data can be modeled assuming a system with two positron-trapping defects. Using the experimentally determined $\tau_V$ (HEA) = 199 ps and $\tau_V$ (iHEA) = 186 ps, and assuming $\tau_{st}$ = 112 ~ 120 ps and $\tau_B$ = 110 ps in both materials, we can fit the temperature behavior of $\tau_{ave}$ in the irradiated samples in the range 50 to 400 K with Eq. (3). The fitting results are shown as the dashed lines in Fig. 2, reproducing the experimental data very well (only two fitted parameters: trapping rates of structural defects and irradiation-induced mono-vacancies). The best fits are found by setting $\tau_{st}$ = 112 ps and n=1.5 for the temperature dependence ($T^{-n}$) of the trapping coefficient of the structural defects in all samples. We note that the behavior of $\tau_1$ is consistent with this model. Due to this effect of the structural defects on the lifetime decomposition (slightly decreasing $\tau_2$ with decreasing temperature), only the data above 200 K are used for determining the average $\tau_2$ in both HEA and iHEA. Similar effects have been observed in Ref. [55].

The fitting gives structural defect trapping rates at 50 K as $\kappa_{st}$ = $2-3\ \lambda_B$ in irradiated HEA and $\kappa_{st}$ = $5-7\ \lambda_B$ in irradiated iHEA, with no dependence on the irradiation fluence. The as-grown data cannot be reliably fitted due to the subtle variation of $\tau_{ave}$ with temperature, but a value of $\kappa_{st}$ not less than that in the irradiated materials is required to reproduce the visible T-dependence. The difference by a factor of 2 – 3 between the two materials suggests that positron diffusion is somewhat enhanced in iHEA, as the structural quality of the HEA and iHEA samples is very similar. The $T^{-1.5}$ dependence of $\kappa_{st}$ leads to values less than 0.3 $\lambda_B$ at elevated temperatures, negligible compared to $\kappa_V$ in higher dose samples, but the positron trapping to these structural defects must be taken into account when analyzing the lower dose data. For the sake consistency, it has been taken into account in the trapping rate fitting in the higher dose samples as well.

Table 1 gives the fitted positron trapping rates to irradiation-induced vacancy defects for the HEA and iHEA samples, as well as the corresponding vacancy concentrations. These allow us to estimate the vacancy concentration as $[V]_{5E15} \approx 5 \times 10^{17}$ cm$^{-3}$ and $[V]_{5E16} \approx 5 \times 10^{18}$ cm$^{-3}$ in as-irradiated HEA and iHEA samples. The introduction rate for mono-vacancies can hence be estimated as $[V]/\phi$ = 100 cm$^{-1}$. This value is an order of magnitude smaller than the prediction by SRIM (1000 cm$^{-1}$), indicating that partial recovery of the irradiation damage takes place already at RT. As the vacancy concentration increases in proportion with the irradiation fluence, we conclude that this RT recovery is simple Frenkel pair recombination without complex defect-defect interactions, as expected at the low irradiation fluxes and fluences used in our experiments.

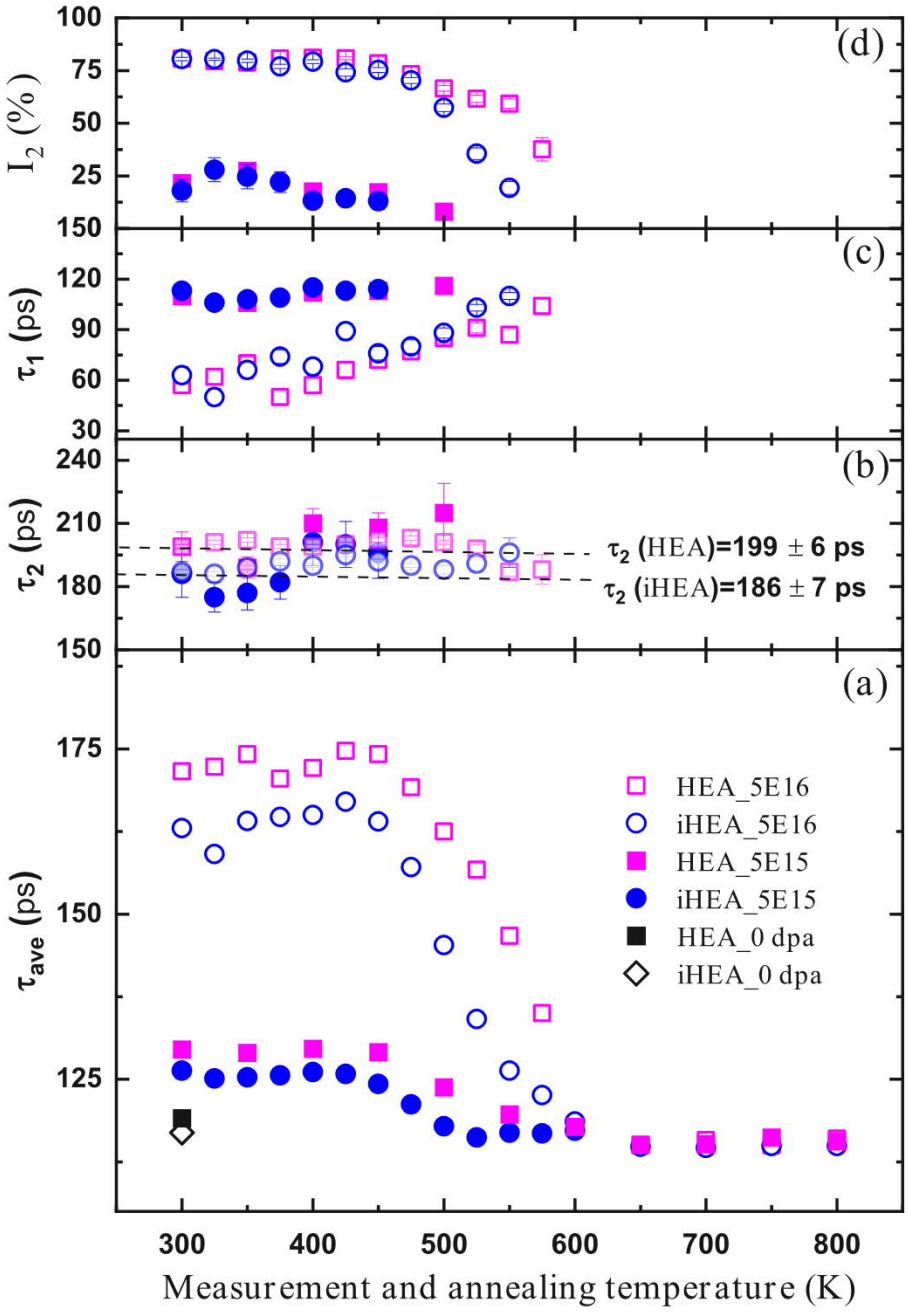


**Fig. 3.** Positron lifetime results as a function of temperature in irradiated samples. The measurements from 300 to 600 K were performed at corresponding temperatures, and the data from 650 to 800 K were measured at RT in between the annealing steps. The average positron lifetime $\tau_{ave}$ is shown in panel (a). The upper panels (b)-(d) show the two lifetime components $\tau_1$ and $\tau_2$ separated from the lifetime spectra, as well as the intensity $I_2$ of the longer lifetime component $\tau_2$.

### *3.2. Thermal recovery of the irradiation-induced vacancy defects*

Fig. 3 shows the positron lifetime obtained in the irradiated HEA and iHEA as a function of measurement and annealing temperature from 300 to 800 K. The RT data for the un-irradiated samples is shown for reference. It is clearly seen that the thermal recovery process starts at around 450 K. Above this temperature, the average positron lifetime gradually decreases, and the original state of the samples as monitored by positron annihilation ($\tau_{ave}$ in the range 115 – 120 ps) is reached by 600 K in both HEA and iHEA samples. This is a direct indication of thermal recovery of the irradiation damage through removal of the irradiation-induced open volume defects. Interestingly, the thermal recovery process appears to take place at slightly lower temperatures in iHEA than in HEA, suggesting improved mobility of point defects in iHEA. Further examination of Fig. 3a reveals that the thermal recovery process begins at the same temperature (about 450 K) in both iHEA and HEA, but the evolution is faster with increasing temperature in iHEA than in HEA. During the recovery process (between 450 K and 600 K), the $I_2$ and $\tau_2$ data (Figs. 3b and 3d) indicate that the recovery process consists of the removal of the irradiation-induced vacancy defects and that the size of these vacancy defects does not change during the recovery process. The latter observation is based negligible evolution of $\tau_2$ in the temperature range 300 – 550 K (increasing on the average by 0.3 ps in HEA and 3 ps in iHEA based on the statistically accurate $\tau_2$ data) of the higher fluence samples. We note that both increases are smaller than the scatter of the data and the individual statistical errors on the data points,

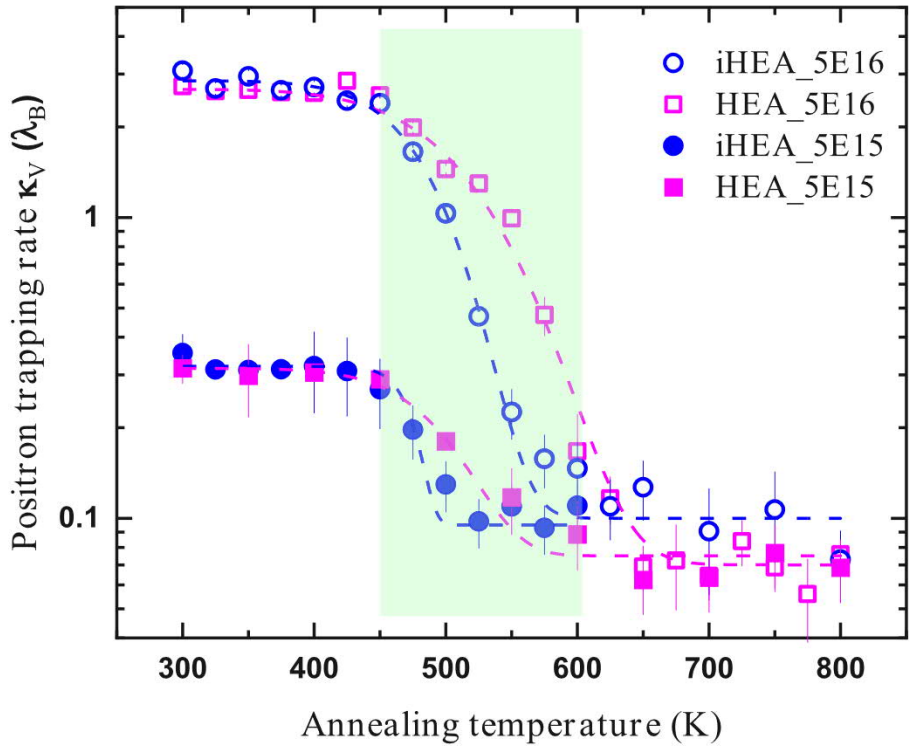


**Fig. 4.** Positron trapping rate ($\kappa_v$) at irradiation-induced mono-vacancies as a function of annealing temperature in irradiated samples. The dashed curves show the fit of the model describing the isochronal annealing process.

hence indicating that $\tau_2$ is constant throughout the thermal recovery process. Further, the higher fluence data indicate that the difference between HEA and iHEA originates from faster removal of the vacancy defects in iHEA. We also note that $\tau_1$ behaves consistently with this picture. Also, it is somewhat too high to be explained by Eq. (1), as expected due the presence of the shallow positron traps discussed in the previous section.

Fig. 4 shows the positron trapping rate at irradiation-induced mono-vacancies ($\kappa_v$) extracted using Eq. (3) from the positron data (Fig. 3) in the post-irradiation annealing temperatures 300 – 800 K. We fit an activation energy $E_A$ of the thermal recovery of the irradiation-induced vacancy defects to the vacancy concentration values that have been determined from positron data, similar as in Refs. [35,63]. The isochronal annealing of the defect concentration $[V]$ can be described as follows [64]:

$$[V]_{i+1} = [V]_\infty + ([V]_i - [V]_\infty) exp(-\nu t \cdot exp(-E_A/(k_B T_i))) \quad (4)$$

where the subscript $i$ denotes the annealing step ($T_i = [300 + 25 \times (i-1)]$ K), $t = 18000$ s is the annealing time, $k_B$ is Boltzmann constant, $\nu = 10^{13}$ s$^{-1}$ is a frequency factor and assumed to be constant, $[V]_\infty$ is the decreased defect concentration due to annealing. In the case where a single activation energy does not describe the behavior sufficiently well, we use $E_A = E_{A_0} + \alpha(T_i - T_1)$ as the activation energy where the parameter $\alpha$ allows the activation energy ($E_A$) to evolve linearly as a function of the annealing temperature.

A single activation energy can be fitted to the iHEA data of both low and high fluence, giving $E_A^V$(iHEA_5E15) $\approx 1.63 \pm 0.02$ eV and $E_A^V$(iHEA_5E16) $\approx 1.64 \pm 0.02$ eV. A single activation energy is an indication of a simple recovery process limited only by the migration barrier of the species annealing out, hence this value of $E_A$ is interpreted as the migration barrier of mono-vacancies in the iHEA samples. In the HEA samples, however, the trapping rate data could not be reproduced with a single activation energy. Allowing the activation energy to evolve with temperature, the HEA data can be fitted with an activation energy that ranges from 1.6 eV to 1.9 eV in the temperature range 450 K – 550 K ($\alpha$ fitted as 0.0023 in the model), implying that the mono-vacancies anneal out in several overlapping stages in this temperature range. Interestingly, the lowest activation energy coincides with the single mono-vacancy migration barrier found in iHEA.

### 3.3. Lattice location of C and N interstitials in HEA and the local lattice distortions

We performed state-of-the-art DFT calculations to determine the preferred sites for C and N interstitials. An example of the employed randomized equiatomic supercells is shown in Fig. 5a. For both the C and N cases, 100 randomly chosen octahedral sites were calculated (see Supplementary Figure 2). The local atomic environment is determined by counting the number of elements in the 6 1$^{st}$ nearest-neighbor (1NN) and 14 1$^{st}$ and 2$^{nd}$ nearest-neighbor (1&2NN) atoms as shown in Fig. 5b. Fig. 6 shows the histograms of the counting distributions and the formation energy distributions for both C and N interstitials in 5 different elemental surroundings. A clear tendency of increasing formation energy for both C and N interstitials with increasing number of Ni atoms in the surroundings, as well as a clear tendency of decreasing formation energy with increasing number of Cr atoms, is visible in Fig. 6.

The slopes of linear fitting are shown in Table 2, where we have also employed the Spearman rank-order coefficient [65] $R_S$ to quantitatively characterize the correlations (values given in bold denote the highest fidelity). In addition to the opposite tendencies for Cr and Ni rich surroundings, also an increase in the number of Mn atoms surrounding the C or N interstitials decreases the formation energy. The results for Fe and Co differ more and they also exhibit larger statistical uncertainty for the two types of interstitials, but generally there appears to be a tendency for increasing formation energy with Co rich surroundings and decrease with Fe rich surroundings. In short, the linear correlation analysis indi-

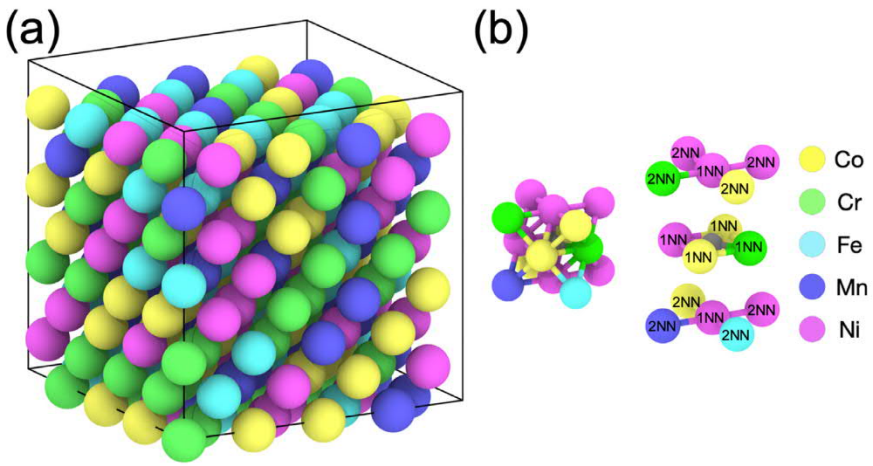


**Fig. 5.** Exemplary 256-atoms equiatomic supercell and octahedral interstitial sites. Six 1st nearest neighbors (1NNs) and eight 2nd nearest neighbors (2NNs) surrounding the interstitial atoms were used to determine the local atomic environment.

**Table 2**
Statistical summary of the DFT calculations. Spearman correlation coefficients $R_S$, P-value, the slope of the linear fitting and the residues of the linear fitting (the measure of the scatter). The bold numbers indicate strong correlation. The P-value is defined as the probability of an uncorrelated system producing datasets that have a Spearman correlation which is equal or larger than the one computed from the actual datasets.

| Element | C interstitials 1NN | | | | C interstitials 1&2NN | | | |
|---|---|---|---|---|---|---|---|---|
| | Spearman $R_S$ | P-value | Slope of linear fitting | Residues of linear fitting | Spearman $R_S$ | P-value | Slope of linear fitting | Residues of linear fitting |
| Co | 0.054 | 0.596 | 0.023 | 7.535 | 0.036 | 0.720 | 0.005 | 7.587 |
| Cr | **-0.231** | 0.021 | -0.086 | 6.807 | **-0.179** | 0.075 | -0.043 | 7.143 |
| Fe | **-0.213** | 0.034 | -0.049 | 7.398 | -0.066 | 0.513 | -0.008 | 7.579 |
| Mn | **-0.150** | 0.138 | -0.034 | 7.500 | -0.094 | 0.354 | -0.012 | 7.559 |
| Ni | **0.513** | 0.000 | 0.139 | 5.738 | **0.369** | 0.000 | 0.071 | 6.607 |
| | N interstitials 1NN | | | | N interstitials 1&2NN | | | |
| Co | **0.376** | 0.000 | 0.124 | 13.193 | **0.229** | 0.022 | 0.066 | 14.390 |
| Cr | **-0.523** | 0.000 | -0.214 | 9.144 | **-0.315** | 0.001 | -0.117 | 12.214 |
| Fe | 0.057 | 0.571 | 0.044 | 14.992 | 0.004 | 0.970 | 0.0014 | 15.186 |
| Mn | **-0.383** | 0.000 | -0.125 | 13.536 | **-0.249** | 0.013 | -0.055 | 14.748 |
| Ni | **0.524** | 0.000 | 0.258 | 9.801 | **0.436** | 0.000 | 0.134 | 12.335 |

cates preferential localization of C/N interstitials in regions rich in Mn and Cr, while clearly avoiding Ni-rich regions. Our calculations are in line with recent experimental evidence that suggests Cr to have the highest affinity towards N interstitials [66] in equiatomic FeMnNiCoCr.

Fig. 7 shows the effects of N interstitials on the local bond distortion distribution in Cr-rich environment, where they are expected to be the most significant due to the preferential localization. The data clearly show that bond distortions behave as expected and similar to that in dilute alloys: the bond distortion distribution becomes wider for all elements. The effect is strongest for Cr as it is over-represented in the 1st nearest neighbors – detailed analysis shows the most significant effects on the local bond distortions are found in the 1st and 2nd nearest neighbors, as expected. We note that our calculations without the interstitials reproduce the local bond distortion distribution shown in Ref. [52]. Cr and Mn exhibit the widest distributions of local bond distortions. The overall rank order of the distortions is Cr>Mn>Fe>Co>Ni.

## 4. Discussion

Our direct monitoring of the thermal recovery of irradiation-induced mono-vacancies in the HEA and iHEA samples leads to the conclusion that the mono-vacancy migration barriers are generally in the range 1.6 – 1.9 eV in equiatomic FeMnNiCoCr. That the migration barriers exhibit a distribution instead a single value is natural due to local fluctuations of elements surrounding the irradiation induced vacancies in a random alloy. The energetics of mono-vacancy migration can also be extracted from elemental diffusion experiments that have been performed in similar HEAs by employing isotope-controlled bulk tracers [67] and diffusion couples [68,69]. The elemental diffusion activation energies determined in these experiments vary from element to element in the range 2.8 – 3.2 eV [67], 3.0 – 3.3 eV [68] and 3.2 – 3.5 eV [69]. The mono-vacancy formation enthalpy has been determined experimentally with positron annihilation as 1.7 ± 0.2 eV in equiatomic FeMnNiCoCr [56], but there is no elemental information that could be extracted as in experiments the identity of the missing atom from the vacant lattice site is not known. Assuming the elemental diffusion to proceed via the vacancy mechanism, the above-listed experimental diffusion activation energy ranges correspond to vacancy migration barrier ranges of 1.1 – 1.5 eV, 1.3 – 1.6 eV, and 1.5 – 1.8 eV (with an overall additional uncertainty of at least ± 0.2 eV), respectively. Our values are in excellent agreement with those obtained from Ref. [69], and somewhat higher than in Refs. [67,68]. Both in our experiments and in the diffusion experiments the distribution of the obtained values is the same with a 0.3 – 0.4 eV range.

Mono-vacancy migration barriers have also been studied employing theoretical calculations. The predicted values in equiatomic FeMnNiCoCr for different elemental vacancies exhibit a range of 0.3 – 0.5 eV irrespective of the employed method [68,70–73], but the modeling predicts systematically lower values (by 0.5 – 1.0 eV) [70,71] than those found in most of the experiments, including ours. The well-known delocalization error from approximated functionals [74] is a likely source of systematic differences between theory and experiment, but the comparison is challenging

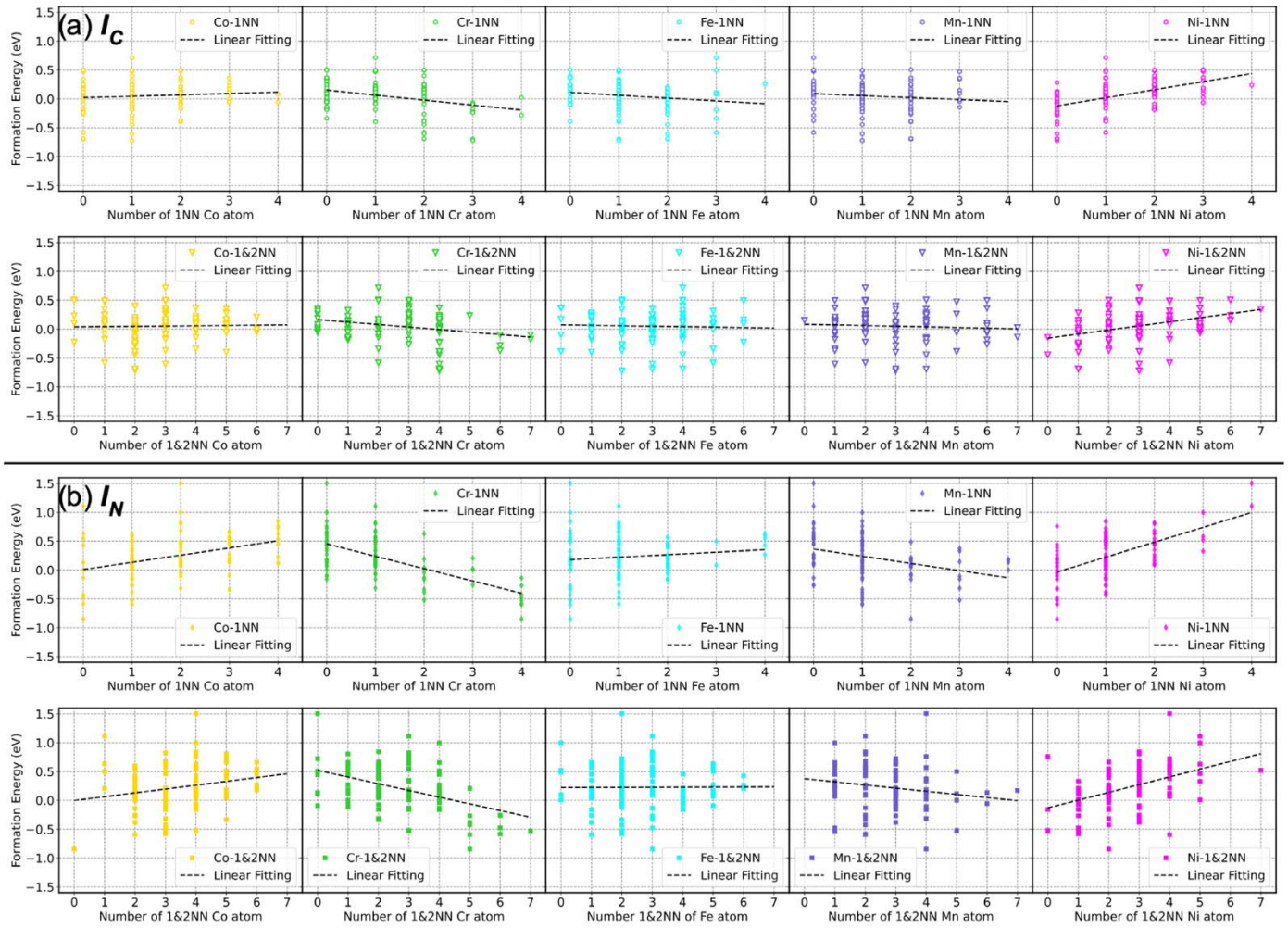


**Fig. 6.** Interstitial formation energy of (a) $l_C$ and (b) $l_N$ vs. the number of certain neighboring elements in the surroundings. As a quantitatively characterization, the Spearman rank-order coefficients, $R_S$ is used to describe the correlation tendency and the slope of the linear fitting is used to extract the dependency of the formation energy on the number of certain elements in the surroundings, as shown in Table 2.

also due to nature of the random alloy itself. First, we note that direct comparison between our experiments and the published theoretical work is not straightforward. In modeling, the vacancies are typically defined by the atom that has been removed from its lattice site, while in our experiments it is not possible to identify which atoms is missing from the vacant lattice site. Interestingly, the mono-vacancy migration barrier in pure Ni has been determined experimentally as 1.1 – 1.3 eV [57,75,76], and theory predicts values that are in excellent agreement with experiments [77]. The theoretically calculated mono-vacancy migration barriers are shown to slightly increase when Ni is alloyed with Fe or Co (equiatomic binary alloys) [77], but in the multi-component alloys the predicted mono-vacancy migration barriers are lower than in elemental Ni [68,70–73]. The scale of diffusion phenomena and the full energy landscape are discussed in Ref. [73] as possible sources of differences between the observations in experiments and the modeling efforts. In our experiments, the mono-vacancies need to migrate a distance of the order of 100 $\mu$m, and in the elemental diffusion experiments the distances are several tens of $\mu$m (slightly longer in diffusion couple than in tracer diffusion experiments). In atomistic modeling, the distances of atomic motion that can be analyzed are several orders of magnitude shorter. Hence it appears that the extracted migration barriers are correlated with the distance traveled by the diffusing species, strongly suggesting that the detailed energy landscape of the random alloys has an important role in determining the migration processes. The longer the distance that the diffusing vacancy (or atom) needs to migrate, the more probable it is that it finds (randomly occurring) regions of higher migration barriers dictated by the immediate atomic surroundings. This is likely to increase the average migration barrier(s) found in experiments, and contribute to the interpretations concerning sluggish diffusion in HEAs in general.

The fact that the mono-vacancy migration barrier range is reduced to a single migration barrier – and to that at the low end of the range – upon the introduction of N and C interstitials in iHEA is unusual and intriguing. C/N interstitials are known to effectively bind to vacancies and significantly increase the migration barriers as, e.g., in b.c.c. Fe, austenitic steel and f.c.c. Ni [25,58,78]. Also in our earlier work [30] the results show that at higher irradiation damage doses (of the order of 1 dpa) and dose rates, it is evident that C interstitials bind to vacancy defects and suppress their mobility. However, when strictly isolated point-like defects are introduced as in our present experiments, the presence of C/N interstitials induces opposite effects. To further discuss this unusual phenomenon, we first summarize the key observations from our experiments and modeling:

1 The irradiation introduces mono-vacancies at the same rate in HEA and iHEA samples.

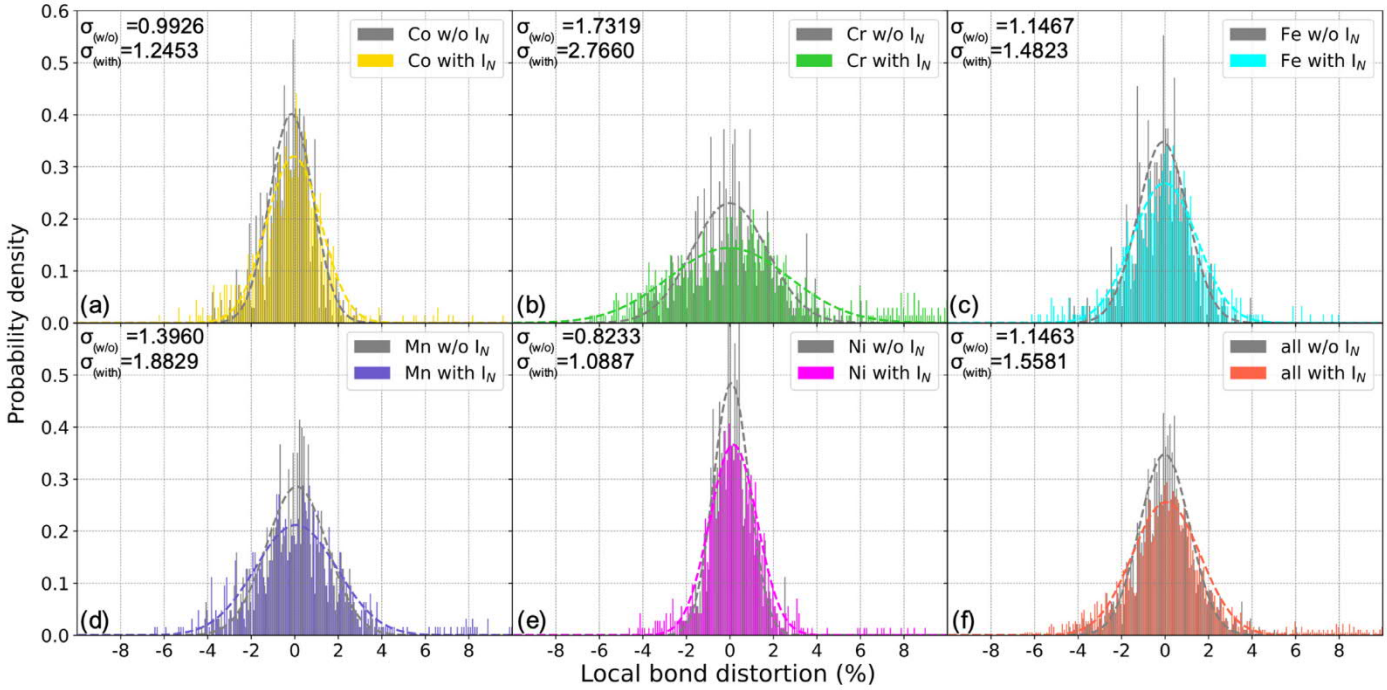


**Fig. 7.** Local bond distortions with and without N interstitials, analyzed from 10 cases with Cr-rich environment (3 or 4 Cr atoms among the 6 1st nearest neighbors). The data show the normalized probability density with the bin-width of 0.1 %.

2 The irradiation-induced mono-vacancies anneal out in thermal treatments on average at lower temperatures in iHEA than in HEA.
3 The mono-vacancy related lifetime stays constant throughout the thermal recovery process in HEA and iHEA.
4 The irradiation-induced mono-vacancies are on average slightly smaller (their positron lifetime is slightly shorter) in iHEA than in HEA.
5 The distribution of activation energies (migration barriers) related to the thermal recovery process is narrower in iHEA, and the distribution narrows towards the lower end of the energy range.
6 Theoretical calculations show that without interstitials, the local lattice distortion distribution is the widest for Cr and Mn. The distributions are symmetrical. Interstitials widen the distributions.
7 Theoretical calculations show that interstitial C and N both prefer Cr and Mn rich regions of the HEA lattice. These are the regions that exhibit the highest distortions (both shorter and longer bonds).

We propose the following mechanism, based on the fundamental chemical disorder in the HEA lattice, to explain our unusual experimental observations. Observations (1), (2) and (3) together imply that, unlike in Fe or Ni [23,25,58,78], the mono-vacancies are not bound to the interstitials in iHEA at any stage of irradiation and thermal treatments, and that we can assume that the irradiation-induced mono-vacancies are randomly (evenly) distributed in the whole lattice in both HEA and iHEA. Due to the lattice distortions, the mono-vacancies in HEA exhibit a distribution of sizes. However, the mono-vacancy size distribution is not symmetric unlike the elemental local bond distortion distributions, as it is bound from below – this distribution has a tail extending to larger sizes. We argue that the preferential localization of the C/N interstitials in the Cr/Mn rich regions of the HEA matrix, that host the largest bond distortions and by consequence the largest and smallest mono-vacancies, effectively narrows the mono-vacancy size distribution. As the C/N interstitials push away the atoms in the 1st and 2nd neighboring cells and the mono-vacancies are on the average 2 – 3 bond lengths from the interstitials (based on the statistics of 1% interstitial concentration), the mono-vacancies end up being smaller on average. At the same time, the large-size tail of the mono-vacancy size distribution is removed as the interstitials occupy the space where the largest mono-vacancies would have been introduced in the irradiation. Note that our data does not exclude the possibility of a small fraction (statistics suggests less than a percent) of the irradiation-induced mono-vacancies to be bound to the C/N interstitials – their concentration would be low enough to not be distinguished from the open volume defects existing in the samples prior to irradiation. The interstitial-induced narrowing and reduction of the mono-vacancy size distribution leading to the narrowing and reduction of the migration barrier distribution implies that mono-vacancy migration is strongly size-dependent in HEA.

The fact that the nature of the atomic-scale chemical disorder and its effects on the local lattice distortions are a decisive factor determining the elemental motion in HEAs might not be surprising, but needs to be taken into account when developing microscopic theories of solute strengthening. The effective and unusual homogenization of the mono-vacancies and their motion in iHEA is opposite to the phenomena found in traditional dilute alloys. We note that our results and the proposed mechanism do not provide a clear distinction between the effects of the C or N interstitials. Both are present at 0.6 – 0.8 at. % in our iHEA samples, and theoretical calculations predict their general behavior to be very similar from the point of view of lattice site energetics in varying atomic surroundings. Our earlier results on the irradiation response of C interstitial containing FeMnNiCoCr [30] suggest that C interstitials alone can lead to the reduction of the total open volume contained in the defects introduced by the irradiation, but the magnitude of that effect cannot be reliably compared to the present results due to the different scale of the experiments. As the concentrations of both C and N interstitials are rather low in our iHEA samples, it is unlikely that they would significantly interact with each other in

irradiation damage and thermal recovery processes. Incorporating a detailed understanding of the effective strain landscape variation mechanism by these and other foreign interstitials (e.g., O) should profoundly benefit the development of HEA engineering strategies.

## 5. Summary

In this work, we report unusual homogenization of vacancy diffusion properties in the equiatomic FeMnNiCoCr high entropy alloy doped with C and N interstitials (iHEA). We present direct experimental evidence of an unexpected interstitial-induced reduction and narrowing of migration barriers of mono-vacancy defects introduced by particle irradiation in the iHEA. The phenomenon is attributed to the preferential localization of C/N interstitials in naturally occurring atomic scale Mn and Cr rich regions of the random alloy predicted by state-of-the-art theoretical calculations. The conclusions obtained by efficient combination of independent experiments and modelling open a pathway for understanding the effect of foreign interstitials on solute strengthening and mechanical properties under irradiation in high entropy alloys.

## Declaration of Competing Interest

The authors declare that they have no known competing financial interests or personal relationships that could have appeared to influence the work reported in this paper.

## Acknowledgment

This work was financial supported by the Academy of Finland (Project Nos. 285809, 315082, 319178 and 321659). CSC—IT Center for Science, Finland, is acknowledged for providing the computational resources. The work done at SUSTech was supported by the High-level University Fund (G02236002 and G02236005). This computational work was supported by the Center for Computational Science and Engineering at Southern University of Science and Technology. The author (Z.L.) would like to acknowledge the financial support by the National Natural Science Foundation of China (Project No. 51971248) and the Special Funding for the Construction of Innovative Hunan Province (2019RS1001).

## Supplementary materials

Supplementary material associated with this article can be found, in the online version, at doi:10.1016/j.actamat.2021.117093.

## References

[1] C.R. LaRosa, M. Shih, C. Varvenne, M. Ghazisaeidi, Solid solution strengthening theories of high-entropy alloys, Mater. Charact. 151 (2019) 310–317, doi:10.1016/j.matchar.2019.02.034.
[2] F. Tuomisto, I. Makkonen, J. Heikinheimo, F. Granberg, F. Djurabekova, K. Nordlund, G. Velisa, H. Bei, H. Xue, W.J. Weber, Y. Zhang, Segregation of Ni at early stages of radiation damage in NiCoFeCr solid solution alloys, Acta Mater. 196 (2020) 44–51, doi:10.1016/j.actamat.2020.06.024.
[3] R.O. Ritchie, The conflicts between strength and toughness, Nat. Mater. 10 (2011) 817–822, doi:10.1038/nmat3115.
[4] B. Cantor, I.T.H. Chang, P. Knight, A.J.B. Vincent, Microstructural development in equiatomic multicomponent alloys, Mater. Sci. Eng. A. 375 (2004) 213–218, doi:10.1016/j.msea.2003.10.257.
[5] J.W. Yeh, S.K. Chen, S.J. Lin, J.Y. Gan, T.S. Chin, T.T. Shun, C.H. Tsau, S.Y. Chang, Nanostructured high-entropy alloys with multiple principal elements: Novel alloy design concepts and outcomes, Adv. Eng. Mater. 6 (2004) 299–303, doi:10.1002/adem.200300567.
[6] B. Gludovatz, A. Hohenwarter, D. Catoor, E.H. Chang, E.P. George, R.O. Ritchie, A fracture-resistant high-entropy alloy for cryogenic applications, Science 345 (2014) 1153–1158, doi:10.1126/science.1254581.
[7] C. Lu, L. Niu, N. Chen, K. Jin, T. Yang, P. Xiu, Y. Zhang, F. Gao, H. Bei, S. Shi, M.R. He, I.M. Robertson, W.J. Weber, L. Wang, Enhancing radiation tolerance by controlling defect mobility and migration pathways in multicomponent single-phase alloys, Nat. Commun. 7 (2016) 1–8, doi:10.1038/ncomms13564.
[8] D.B. Miracle, O.N. Senkov, A critical review of high entropy alloys and related concepts, Acta Mater. 122 (2017) 448–511, doi:10.1016/j.actamat.2016.08.081.
[9] Z. Li, K.G. Pradeep, Y. Deng, D. Raabe, C.C. Tasan, Metastable high-entropy dual-phase alloys overcome the strength-ductility trade-off, Nature 534 (2016) 227–230, doi:10.1038/nature17981.
[10] O. El-Atwani, N. Li, M. Li, A. Devaraj, J.K.S. Baldwin, M.M. Schneider, D. Sobieraj, J.S. Wróbel, D. Nguyen-Manh, S.A. Maloy, E. Martinez, Outstanding radiation resistance of tungsten-based high-entropy alloys, Sci. Adv. 5 (2019) 1–10, doi:10.1126/sciadv.aav2002.
[11] E. Ma, X. Wu, Tailoring heterogeneities in high-entropy alloys to promote strength–ductility synergy, Nat. Commun. 10 (2019) 1–10, doi:10.1038/s41467-019-13311-1.
[12] C. Varvenne, A. Luque, W.A. Curtin, Theory of strengthening in fcc high entropy alloys, Acta Mater. 118 (2016) 164–176, doi:10.1016/j.actamat.2016.07.040.
[13] H.S. Oh, S.J. Kim, K. Odbadrakh, W.H. Ryu, K.N. Yoon, S. Mu, F. Körmann, Y. Ikeda, C.C. Tasan, D. Raabe, T. Egami, E.S. Park, Engineering atomic-level complexity in high-entropy and complex concentrated alloys, Nat. Commun. 10 (2019) 1–8, doi:10.1038/s41467-019-10012-7.
[14] Z. Wang, I. Baker, Interstitial strengthening of a f.c.c. FeNiMnAlCr high entropy alloy, Mater. Lett. 180 (2016) 153–156, doi:10.1016/j.matlet.2016.05.122.
[15] Z. Li, C.C. Tasan, H. Springer, B. Gault, D. Raabe, Interstitial atoms enable joint twinning and transformation induced plasticity in strong and ductile high-entropy alloys, Sci. Rep. 7 (2017) 40704, doi:10.1038/srep40704.
[16] Z. Lei, X. Liu, Y. Wu, H. Wang, S. Jiang, S. Wang, X. Hui, Y. Wu, B. Gault, P. Kontis, D. Raabe, L. Gu, Q. Zhang, H. Chen, H. Wang, J. Liu, K. An, Q. Zeng, T.G. Nieh, Z. Lu, Enhanced strength and ductility in a high-entropy alloy via ordered oxygen complexes, Nature 563 (2018) 546–550, doi:10.1038/s41586-018-0685-y.
[17] M. Song, R. Zhou, J. Gu, Z. Wang, S. Ni, Y. Liu, Nitrogen induced heterogeneous structures overcome strength-ductility trade-off in an additively manufactured high-entropy alloy, Appl. Mater. Today. 18 (2020) 1–6, doi:10.1016/j.apmt.2019.100498.
[18] Z. Li, Interstitial equiatomic CoCrFeMnNi high-entropy alloys: carbon content, microstructure, and compositional homogeneity effects on deformation behavior, Acta Mater. 164 (2019) 400–412, doi:10.1016/j.actamat.2018.10.050.
[19] W. Zhang, D. Yan, W. Lu, Z. Li, Carbon and nitrogen co-doping enhances phase stability and mechanical properties of a metastable high-entropy alloy, J. Alloys Compd. 831 (2020) 154799, doi:10.1016/j.jallcom.2020.154799.
[20] I. Baker, Interstitials in f.c.c. high entropy alloys, Metals (Basel). 10 (2020) 1–20. doi:10.3390/met10050695.
[21] J.P. Hirth, M. Cohen, On the strength-differential phenomenon in hardened steel, Metall. Trans. 1 (1970) 3–8, doi:10.1007/BF02819235.
[22] R.P. Reed, Nitrogen in austenitic stainless steels, Jom. 41 (1989) 16–21, doi:10.1007/BF03220991.
[23] P. Hautojärvi, J. Johansson, A. Vehanen, J. Yli-Kauppila, P. Moser, Vacancy-Carbon Interaction in Iron, Phys. Rev. Lett. 44 (1980) 1326–1329, doi:10.1103/PhysRevLett.44.1326.
[24] J. Wolff, M. Franz, J.E. Kluin, D. Schmid, Vacancy formation in nickel and $\alpha$-nickel-carbon alloy, Acta Mater. 45 (1997) 4759–4764, doi:10.1016/S1359-6454(97)00112-2.
[25] C. Domain, C.S. Becquart, J. Foct, Ab initio study of foreign interstitial atom (C, N) interactions with intrinsic point defects in $\alpha$-Fe, Phys. Rev. B. 69 (2004) 144112, doi:10.1103/PhysRevB.69.144112.
[26] Y. Ikeda, I. Tanaka, J. Neugebauer, F. Körmann, Impact of interstitial C on phase stability and stacking-fault energy of the CrMnFeCoNi high-entropy alloy, Phys. Rev. Mater. 3 (2019) 68–71, doi:10.1103/PhysRevMaterials.3.113603.
[27] Y. Han, H. Li, H. Feng, K. Li, Y. Tian, Z. Jiang, Enhancing the strength and ductility of CoCrFeMnNi high-entropy alloy by nitrogen addition, Mater. Sci. Eng. A. 789 (2020) 139587, doi:10.1016/j.msea.2020.139587.
[28] F. Xiong, R. Fu, Y. Li, B. Xu, X. Qi, Influences of nitrogen alloying on microstructural evolution and tensile properties of CoCrFeMnNi high-entropy alloy treated by cold-rolling and subsequent annealing, Mater. Sci. Eng. A. 787 (2020) 139472, doi:10.1016/j.msea.2020.139472.
[29] K. Gan, D. Yan, S. Zhu, Z. Li, Interstitial effects on the incipient plasticity and dislocation behavior of a metastable high-entropy alloy: Nanoindentation experiments and statistical modeling, Acta Mater. 206 (2021) 116633, doi:10.1016/j.actamat.2021.116633.
[30] E. Lu, I. Makkonen, K. Mizohata, Z. Li, J. Raisanen, F. Tuomisto, Effect of interstitial carbon on the evolution of early-stage irradiation damage in equi- atomic FeMnNiCoCr high-entropy alloys Effect of interstitial carbon on the evolution of early-stage irradiation damage in equi-atomic FeMnNiCoCr high-entropy alloys, J. Appl. Phys. (2020) 025103, doi:10.1063/1.5130748.
[31] F. Tuomisto, I. Makkonen, Defect identification in semiconductors with positron annihilation: Experiment and theory, Rev. Mod. Phys. 85 (2013) 1583–1631, doi:10.1103/RevModPhys.85.1583.
[32] F.A. Selim, Positron annihilation spectroscopy of defects in nuclear and irradiated materials- a review, Mater. Charact. 174 (2021) 110952, doi:10.1016/j.matchar.2021.110952.
[33] S. Väyrynen, P. Pusa, P. Sane, P. Tikkanen, J. Räisänen, K. Kuitunen, F. Tuomisto, J. Härkönen, I. Kassamakov, E. Tuominen, E. Tuovinen, Setup for irradiation and characterization of materials and Si particle detectors at cryogenic temperatures, Nucl. Instruments Methods Phys. Res. Sect. A Accel. Spectrometers, Detect. Assoc. Equip. 572 (2007) 978–984, doi:10.1016/j.nima.2006.11.065.
[34] J. Slotte, S. Kilpeläinen, F. Tuomisto, J. Räisänen, A.N. Larsen, Direct observations of the vacancy and its annealing in germanium, Phys. Rev. B. 83 (2011) 235212, doi:10.1103/PhysRevB.83.235212.
[35] J. Heikinheimo, K. Mizohata, J. Räisänen, T. Ahlgren, P. Jalkanen, A. Lahtinen,

N. Catarino, E. Alves, F. Tuomisto, Direct observation of mono-vacancy and self-interstitial recovery in tungsten, APL Mater. 7 (2019), doi:10.1063/1.5082150.
[36] R.E. Stoller, M.B. Toloczko, G.S. Was, A.G. Certain, S. Dwaraknath, F.A. Garner, On the use of SRIM for computing radiation damage exposure, Nucl. Instruments Methods Phys. Res. Sect. B Beam Interact. with Mater. Atoms. 310 (2013) 75–80, doi:10.1016/j.nimb.2013.05.008.
[37] P. Hautojärvi, C. Corbel, Positron Spectroscopy of Defects in Metals and Semiconductors, in positron spectroscopy of solids, IOS Press, Amsterdam, 1995, doi:10.3254/978-1-61499-211-0-491.
[38] K. Saarinen, P. Hautojärvi, C. Corbel, Identification of Defects in Semiconductors, Acad. Press, New York, 1998.
[39] J.P. Perdew, A. Zunger, Self-interaction correction to density-functional approximations for many-electron systems, Phys. Rev. B. 23 (1981) 5048–5079, doi:10.1103/PhysRevB.23.5048.
[40] P.E. Blöchl, Projector augmented-wave method, Phys. Rev. B. 50 (1994) 17953–17979, doi:10.1103/PhysRevB.50.17953.
[41] G. Kresse, J. Furthmüller, Efficiency of ab-initio total energy calculations for metals and semiconductors using a plane-wave basis set, Comput. Mater. Sci. 6 (1996) 15–50, doi:10.1016/0927-0256(96)00008-0.
[42] G. Kresse, D. Joubert, From ultrasoft pseudopotentials to the projector augmented-wave method G, Phys. Rev. B. 59 (1999) 1758–1775, doi:10.1103/PhysRevB.59.1758.
[43] G. Kresse, J. Furthmüller, Efficient iterative schemes for ab initio total-energy calculations using a plane-wave basis set, Phys. Rev. B. 54 (1996) 11169–11186, doi:10.1103/PhysRevB.54.11169.
[44] E. Boroński, R.M. Nieminen, Electron-positron density-functional theory, Phys. Rev. B. 34 (1986) 3820–3831, doi:10.1103/PhysRevB.34.3820.
[45] I. Makkonen, M. Hakala, M.J. Puska, Modeling the momentum distributions of annihilating electron-positron pairs in solids, Phys. Rev. B. 73 (2006) 1–12, doi:10.1103/PhysRevB.73.035103.
[46] G. Kresse, J. Hafner, Ab initio molecular dynamics for liquid metals, Phys. Rev. B. 47 (1993) 558–561, doi:10.1103/PhysRevB.47.558.
[47] G. Kresse, J. Hafner, Ab initio molecular-dynamics simulation of the liquid-metalamorphous- semiconductor transition in germanium, Phys. Rev. B. 49 (1994) 14251–14269, doi:10.1103/PhysRevB.49.14251.
[48] J.P. Perdew, A. Ruzsinszky, G.I. Csonka, O.A. Vydrov, G.E. Scuseria, L.A. Constantin, X. Zhou, K. Burke, Restoring the density-gradient expansion for exchange in solids and surfaces, Phys. Rev. Lett. 100 (2008) 1–4, doi:10.1103/PhysRevLett.100.136406.
[49] J.P. Perdew, A. Ruzsinszky, G.I. Csonka, O.A. Vydrov, G.E. Scuseria, L.A. Constantin, X. Zhou, K. Burke, Erratum: Restoring the density-gradient expansion for exchange in solids and surfaces (Physical Review Letters (2008) 100 (136406)), Phys. Rev. Lett. 102 (2009) 39902, doi:10.1103/PhysRevLett.102.039902.
[50] J.D. Pack, H.J. Monkhorst, special points for Brillouin-zone integrations"-a reply, Phys. Rev. B. 13 (1976) 5188–5192, doi:10.1103/PhysRevB.16.1748.
[51] D. Ma, B. Grabowski, F. Körmann, J. Neugebauer, D. Raabe, Ab initio thermodynamics of the CoCrFeMnNi high entropy alloy: Importance of entropy contributions beyond the configurational one, Acta Mater. 100 (2015) 90–97, doi:10.1016/j.actamat.2015.08.050.
[52] H.S. Oh, D. Ma, G.P. Leyson, B. Grabowski, E.S. Park, F. Kormann, D. Raabe, Lattice distortions in the FeCoNiCrMn high entropy alloy studied by theory and experiment, Entropy 18 (2016) 1–9, doi:10.3390/e18090321.
[53] A. Zunger, S.H. Wei, G. Ferreira, Hames E. Bernard, Special Quasirandom Structures, Phys. Rev. Lett. 65 (1990) 353–356, doi:10.1103/PhysRevLett.65.353.
[54] A. Stukowski, Visualization and analysis of atomistic simulation data with OVITO-the Open Visualization Tool, Model. Simul. Mater. Sci. Eng. (2010) 18, doi:10.1088/0965-0393/18/1/015012.
[55] M. Elsayed, R. Krause-Rehberg, C. Eisenschmidt, N. Eißmann, B. Kieback, Defect Study in CoCrFeMnNi High Entropy Alloy by Positron Annihilation Lifetime Spectroscopy, Phys. Status Solidi Appl. Mater. Sci. 215 (2018) 1–4, doi:10.1002/pssa.201800036.
[56] K. Sugita, N. Matsuoka, M. Mizuno, H. Araki, Vacancy formation enthalpy in CoCrFeMnNi high-entropy alloy, Scr. Mater. 176 (2020) 32–35, doi:10.1016/j.scriptamat.2019.09.033.
[57] G. Dlubek, O. Brummer, N. Meyendorf, P. Hautojarvi, A. Vehanen, J. Yli-Kauppila, Impurity-induced vacancy clustering in cold-worked nickel, J. Phys. F Met. Phys. 9 (1979) 1961–1973, doi:10.1088/0305-4608/9/10/007.
[58] A. Vehanen, P. Hautojärvi, J. Johansson, J. Yli-Kauppila, P. Moser, Vacancies and carbon impurities in $\alpha$-iron: Electron irradiation, Phys. Rev. B. 25 (1982) 762–780, doi:10.1103/PhysRevB.25.762.
[59] J. Johansson, A. Vehanen, J. Yli-Kauppila, Positron Lifetime Measurements on Electron-Irradiated Chromium., Radiat. Eff. Lett. 58 (1981) 31–33, doi:10.1080/01422448108226525.
[60] D.E. Jodi, T.A. Listyawan, P. Hruska, J. Cizek, N. Park, U. Lee, Study of vacancies in Fex(CoCrMnNi)100-x medium- and high-entropy alloys by positron annihilation spectroscopy, Scr. Mater. 194 (2021) 9–11, doi:10.1016/j.scriptamat.2020.113654.
[61] S. Abhaya, R. Rajaraman, S. Kalavathi, G. Amarendra, Positron annihilation studies on FeCrCoNi high entropy alloy, J. Alloys Compd. 620 (2015) 277–282, doi:10.1016/j.jallcom.2014.09.137.
[62] K.G. Lynn, C.L. Snead, J.J. Hurst, Positron lifetime studies of pure Ni from 4.2 to 1700K, J. Phys. F Met. Phys. 10 (1980) 1753–1761, doi:10.1088/0305-4608/10/8/012.
[63] D.C. Look, D.C. Reynolds, J.W. Hemsky, R.L. Jones, J.R. Sizelove, Production and annealing of electron irradiation damage in ZnO, Appl. Phys. Lett. 75 (1999) 811–813, doi:10.1063/1.124521.
[64] F. Agulló-López, C.R.A. Catlow, P.D. Townsend, Point Defects in Materials, Academic Press, 1988.
[65] D. Zwillinger, K. Stephen, CRC Standard Probability and Statistics Tables and Formulae, Chapman & Hall, New York, 2000 section 14.7, n.d.
[66] I. Moravcik, J. Cizek, L. de A. Gouvea, J. Cupera, I. Guban, I. Dlouhy, Nitrogen interstitial alloying of CoCrFeMnNi high entropy alloy through reactive powder milling, Entropy 21 (2019) 1–7, doi:10.3390/e21040363.
[67] M. Vaidya, K.G. Pradeep, B.S. Murty, G. Wilde, S.V. Divinski, Bulk tracer diffusion in CoCrFeNi and CoCrFeMnNi high entropy alloys, Acta Mater. 146 (2018) 211–224, doi:10.1016/j.actamat.2017.12.052.
[68] K.Y. Tsai, M.H. Tsai, J.W. Yeh, Sluggish diffusion in Co-Cr-Fe-Mn-Ni high-entropy alloys, Acta Mater. 61 (2013) 4887–4897, doi:10.1016/j.actamat.2013.04.058.
[69] J. Dąbrowa, M. Zajusz, W. Kucza, G. Cieślak, K. Berent, T. Czeppe, T. Kulik, M. Danielewski, Demystifying the sluggish diffusion effect in high entropy alloys, J. Alloys Compd. 783 (2019) 193–207, doi:10.1016/j.jallcom.2018.12.300.
[70] W.M. Choi, Y.H. Jo, S.S. Sohn, S. Lee, B.J. Lee, Understanding the physical metallurgy of the CoCrFeMnNi high-entropy alloy: An atomistic simulation study, Npj Comput. Mater. 4 (2018) 1–9, doi:10.1038/s41524-017-0060-9.
[71] M. Mizuno, K. Sugita, H. Araki, Defect energetics for diffusion in CrMnFeCoNi high-entropy alloy from first-principles calculations, Comput. Mater. Sci. 170 (2019) 109163, doi:10.1016/j.commatsci.2019.109163.
[72] J. Kottke, D. Utt, M. Laurent-Brocq, A. Fareed, D. Gaertner, L. Perrière, Ł. Rogal, A. Stukowski, K. Albe, S.V. Divinski, G. Wilde, Experimental and theoretical study of tracer diffusion in a series of (CoCrFeMn)100−xNix alloys, Acta Mater. 194 (2020) 236–248, doi:10.1016/j.actamat.2020.05.037.
[73] S.L. Thomas, S. Patala, Vacancy diffusion in multi-principal element alloys: The role of chemical disorder in the ordered lattice, Acta Mater. 196 (2020) 144–153, doi:10.1016/j.actamat.2020.06.022.
[74] A.J. Cohen, P. Mori-Sanchez, W. Yang, Insights into Current Limitations of Density Functional Theory, Science 321 (2008) 792–794, doi:10.1126/science.1158722.
[75] L.C. Smedskjaer, M.J. Fluss, D.G. Legnini, M.K. Chason, R.W. Siegel, The vacancy formation enthalpy in Ni determined by positron annihilation, J. Phys. F Met. Phys. 11 (1981) 2221–2230, doi:10.1088/0305-4608/11/11/005.
[76] W. Wycisk, M. Feller-Kniepmeier, Quenching experiments on high-purity nickel, Phys. Status Solidi. 37 (1976) 183–191, doi:10.1002/pssa.2210370124.
[77] S. Zhao, G.M. Stocks, Y. Zhang, Defect energetics of concentrated solid-solution alloys from ab initio calculations: Ni0.5Co0.5, Ni0.5Fe0.5, Ni0.8Fe0.2 and Ni0.8Cr0.2, Phys. Chem. Chem. Phys. 18 (2016) 24043–24056, doi:10.1039/c6cp05161h.
[78] D.J. Hepburn, D. Ferguson, S. Gardner, G.J. Ackland, First-principles study of helium, carbon, and nitrogen in austenite, dilute austenitic iron alloys, and nickel, Phys. Rev. B. 88 (2013) 024115, doi:10.1103/PhysRevB.88.024115.